Mechanics and stability of vesicles and droplets in confined spaces

Eduard Benet and Franck J. Vernerey[*]

Department of Mechanical Engineering, University of Colorado Boulder, Boulder, Colorado 80309-0427, USA
(Received 29 September 2016; published 29 December 2016)

The permeation and trapping of soft colloidal particles in the confined space of porous media are of critical importance in cell migration studies, design of drug delivery vehicles, and colloid separation devices. Our current understanding of these processes is however limited by the lack of quantitative models that can relate how the elasticity, size, and adhesion properties of the vesicle-pore complex affect colloid transport. We address this shortcoming by introducing a semianalytical model that predicts the equilibrium shapes of a soft vesicle driven by pressure in a narrow pore. Using this approach, the problem is recast in terms of pressure and energy diagrams that characterize the vesicle stability and permeation pressures in different conditions. We particularly show that the critical permeation pressure for a vesicle arises from a compromise between the critical entry pressure and exit pressure, both of which are sensitive to geometrical features, mechanics, and adhesion. We further find that these results can be leveraged to rationally design microfluidic devices and diodes that can help characterize, select, and separate colloids based on physical properties.

I. INTRODUCTION

The separation and trapping of micron-sized and nanosized colloidal particles by porous media have been and still are the object of a number of studies with important outcomes in a variety of disciplines. In chemical engineering and the food industry [1], efficient filtration processes heavily depend on the design of membranes targeting colloidal particles [2] and their treatment on the formation of cakes [3,4]. In medicine, effective strategies to capture circulating tumor cells (CTCs) in the bloodstream could enable the detection of certain forms of cancer at an early stage and improve treatment with patient-specific therapies [5,6]. To address those needs, researchers and engineers have developed a large spectrum of microfluidics [7], membranes [8], and experimental techniques [9] aimed to capture and separate colloidal particles, most of them using particle size as the segregation criterion.

Separation based on the physical properties of particles, such as deformability and adhesion or wetting, is however less common. In spite of our limited understanding of these processes, recent techniques have been devised based on the apparent correlation between colloid properties (surface tension and particle elasticity) and their ability to permeate through narrow pores. These techniques could indeed be critical in the separation and trapping of particles with similar sizes but different properties, which include, for instance, CTCs and leucocytes [10]. In this context, efforts have focused on microfluidic devices that possess gradual variations in pore size [11] such that particles of distinct mechanical properties can be separated [12] or trapped [13] depending on their position in the device. Recently, studies by Sarioglu *et al.* [14] and McFaul *et al.* [15] have further shown that pore shape can be used as a design criterion for particle separation. These studies indeed showed that anisotropic pores or microfluidic diodes [16] could act as valves allowing deformable particles to travel in only one direction. One key lesson from these studies

is that deformability, in addition to size, should be considered in the design of filtration membranes and microfluidic devices. However, particle separation is not the sole application of these technologies; the critical pressure and deformation of a particle in a nanopore (or channel) may also be used to learn about its mechanical response. For instance, Evans and Yeung [17] proposed the use of a micropipette aspiration test to determine the surface tension, membrane elasticity, and/or viscosity of soft colloids. This technique is now considered as a standard [18] for quantifying the mechanics of a variety of particles including cells [19] and vesicles [20]. Variations of this strategy have also been proposed, including, for instance, the use of conical microchannels to determine the elastic properties of bacteria based on their equilibrium position under a pressure gradient [21].

A number of theoretical studies have been proposed to understand and guide experimental efforts but to date have exclusively targeted the critical pressure that is necessary for a particle to enter a pore. These include the derivation of analytical expressions relating surface tension and elasticity to the entry of a vesicle in a cylindrical channel mimicking a micropipette [18] or anopore membranes [22]. An extension to noncircular openings was also proposed analytically by Bruus [23] for more complex pore shapes. However, when more complex pore or vesicle shapes are considered, solutions must be derived numerically as discussed by Leong *et al.* [24] in the context of vesicle properties and Zhang *et al.* [25] in the context of pore shapes. Besides deformability, the physical interactions between a pore and a particle, particularly their mutual adhesion, are also known to be an important factor in the permeation problem [26], but surprisingly studies on this topic are scarce in the literature. Indeed, while the physics of adhesion between a vesicle and a substrate is widely known, it was not until the work of Fournier and Galatola [27] that it was applied to the permeation of a vesicle through axisymmetric pores of varying cross sections (both cylindrical and conical). Using an enhanced version of the Laplace law accounting for both the bending stiffness and the adhesion of a lipid membrane, the authors derived relationships between the pressure applied along the channel and the shape acquired by

---

[*]franck.vernerey@colorado.edu; https://vernereygroup.wordpress.com

a vesicle. The relationship between entry pressure, permeation pressure, and the deformability, size, and adhesion energy of a colloidal particle in an arbitrary pore is however still poorly understood.

In this work we propose to fill this gap by adopting a semianalytical approach that considers the interactions of a vesicle characterized by its surface tension, size, and adhesion energy with an axisymmetric pore of arbitrary cross section. We particularly aim at understanding the interplay between pore geometry and particle adhesion on the physics of vesicle permeation, which includes the phenomena of entry, exit, and trapping within pores. Results are presented in terms of pressure and energy diagrams that enable the visualization of the various mechanical instabilities undergone by a vesicle traveling through a pore and how they are affected by pore aperture, curvature, and asymmetry. We further show that the exit pressure, in addition to entry pressure, is a key feature for the permeation of moderately adhesive particles.

II. EQUILIBRIUM MECHANICS OF A VESICLE IN A PORE

We concentrate here on a class of deformable particles, or vesicles, whose structure can be represented by an inner fluid surrounded by a thin viscous membrane with surface tension γ. Such a system constitutes a generic model for a variety of living and nonliving particles including cells, liposomes, droplets, or microbubbles. Note that although this approach is exact for immiscible fluid droplets, it is usually not the case for particles coated by a thin shell (lipids, for instance). In this case, areal extension can arise from two different phenomena: (a) a stretch of thermal fluctuations associated with a rise in surface tension [28] as seen in liposomes [29] and (b) the unfolding of excess area stored in the membrane in the form of wrinkles [17]. This has been observed in the deformation of neutrophils wherein the change in tension was negligible [30]. We further note that in the case where a vesicle is not spherical, the approach should incorporate the effect of the lipid shell bending rigidity κ [31,32]. Thus, in general, Helfrich [33] has shown that a vesicle at equilibrium possesses a pressure drop across its interface ΔP_I that depends on the membrane properties as

$$\Delta P_I = 2\gamma H - 2\kappa[2H(H^2 - K) - \Delta_s H], \qquad (1)$$

where H and K are the mean and Gaussian curvatures on the membrane, respectively, and Δ_s is the surface Laplacian operator. Fully solving the immersed membrane problem usually requires a sophisticated numerical approach such as that proposed by Foucard *et al.* [34]. For simplicity, the present approach considers the case of apparently spherical vesicles that possess small surface fluctuations that can stretch under force. In this case, as pointed out by Fournier and Galatola [27], Eq. (1) degenerates to the classical Laplace law $\Delta P_I = 2\gamma H$ when the minimum radius of curvature verifies $R \gg \sqrt{\kappa/\gamma}$. Thus, for a majority of apparently spherical vesicles whose surface tension is on the order of $10^{-3}\,\text{N/m}$ [35] and bending resistance $\kappa \approx 10^{-19}\,\text{N m}$ [36] the Laplace law holds for radii larger than a critical value $R_c = 0.1\,\mu\text{m}$. For microbubbles however, the surface tension and bending modulus are on the order of $10^{-2}\,\text{N/m}$ [37] and $10^{-19}\,\text{Nm}$
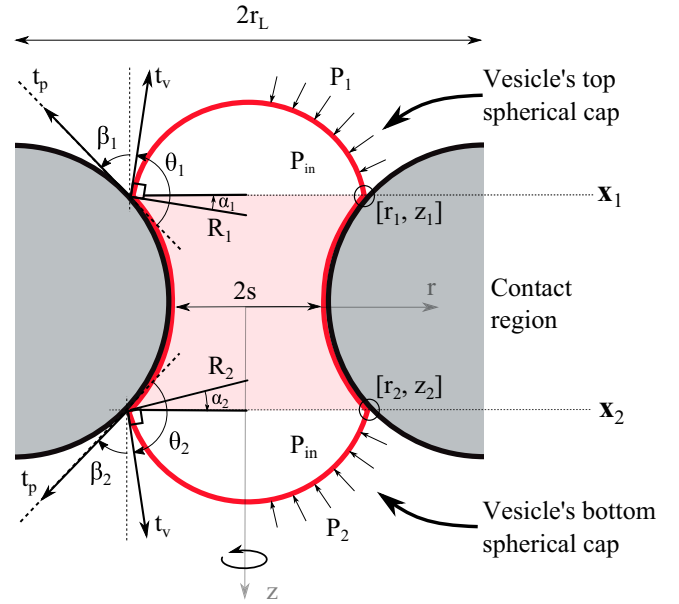

FIG. 1. Scheme of a vesicle in equilibrium due to a pressure difference $P_1 - P_2$ in an axisymmetric pore with minimum aperture radius s. The vesicle is divided in three parts by the two contact lines $\mathbf{x}_1 = [r_1, z_1]$ and $\mathbf{x}_2 = [r_2, z_2]$: two spherical caps with radii R_1 and R_2 and the contact region in between. The spherical caps meet the pore at the contact line i with an angle of θ, which is defined by the tangent at the pore $\mathbf{t}_p$ and the vesicle $\mathbf{t}_v$. The volume of each cap is defined by their radius inner angle α_i between the horizontal and the radius at the detachment point. These magnitudes are all related by the angle that the pore tangent makes with the vertical β_i, defined as positive counterclockwise in the top cap and clockwise in the bottom one.

[38], respectively, and the Laplace approximation is restricted to smaller critical radii, near $R_c = 0.01\,\mu\text{m}$. The case of cells is however more complex since the presence of the cortex gives them a viscoelastic behavior [39] in both stretching and bending. Hence, this approach is only valid in cases where the deformation is purely due to the membrane unfolding as observed in the micropipette aspiration of neutrophils [40].

Let us consider an incompressible vesicle of radius $R > R_c$ trapped in an axisymmetric pore whose smallest aperture is $s < R$ (Fig. 1). At equilibrium, the deformation of this vesicle depends on the pressure drop across the pore $\Delta P = P_2 - P_1$, the surface tension of the vesicle γ, and its contact angle with the pore θ ($\frac{\pi}{2} < \theta < \pi$ for partially wetting vesicles [41]). Contact angles below $\pi/2$ would imply a preference for the vesicle to wet the pore by splitting and/or sticking to the side of the pore surface [42]. This situation is fundamentally different from the objective of our study and is therefore not considered. For small capillary numbers [18] and in the absence of body forces, the morphology of the vesicle can be divided into three sections: two free spherical caps whose curvatures ρ_1 and ρ_2 are determined by the Laplace law $\rho_i = (P_i - P_{in})/2\gamma$, with P_{in} the internal vesicle pressure, and a confined section (shaded in Fig. 1) whose geometry is restricted by the pore shape. Mathematically, these regions are characterized by the coordinates of two contact lines $\mathbf{x}_1 = [r_1, z_1]$ and $\mathbf{x}_2 = [r_2, z_2]$ and the pore shape parametrization $\mathbf{x} = [r(z), z]$, where (r, z)

are cylindrical coordinates about a system whose origin is at the center of the pore. The global equilibrium of the vesicle can be easily derived by taking the difference between ρ_2 and ρ_1 in order to obtain

$$\Delta P = 2\gamma(\rho_2 - \rho_1). \qquad (2)$$

Note that this expression is only valid for equilibrium or quasistatic systems in which the inner vesicle pressure is homogeneous and there is no fluid flow around the pore. A dynamic approach would require solving the Navier-Stokes equations coupled with the membrane governing equations [43]. By simple geometrical relations, one can show that the cap curvatures can be related to the pore geometry by $\rho_i = -\cos(\theta + \beta_i)/r_i$, where r_i and $\beta_i = \arctan[r'(z_i)]$ are the radii and the signed tangent angle (with $r' = dr/dz$) of each contact lines (Fig. 1). Using the Young-Dupre relation [41], the contact angle can further be related to the adhesion energy Γ between the vesicle and the pore by $\cos(\theta) = -\Gamma/\gamma - 1$, allowing us to express the cap curvatures in terms of the surface energy as

$$\rho_i = \frac{1}{\gamma r_i}\left[\gamma \cos \beta_i + \Gamma\left(\cos \beta_i + \sin \beta_i \sqrt{-1 - 2\frac{\gamma}{\Gamma}}\right)\right]. \qquad (3)$$

This relation, together with Eq. (2), can be used to compute the pressure drop across a vesicle in a pore, as long as one knows the position of the contact lines $\mathbf{x}_1$ and $\mathbf{x}_2$. It can be useful, for instance, to characterize the tendency of a vesicle to enter a pore by measuring its sudden pressure drop ΔP as it first makes contact with the pore surface. At this point, the two contact lines are confounded (i.e., $r_1 = r_2$ and $\beta_1 = -\beta_2$) and we are left with the term $\Delta P = 4 \sin(\beta_1)\frac{\Gamma}{r_1}\sqrt{-1 - 2\frac{\gamma}{\Gamma}}$, which measures the *suction pressure* that drives a vesicle into the pore. A simple observation of this equation show that this pressure increases with adhesion energy Γ and pore orientation angle β_1 but decreases with the contact line radius r_1.

It can also be seen that, taking $\beta_1 = \frac{\pi}{2}$, $\beta_2 = 0$, and $r_2 = s$, (3) directly yields the formula proposed by Fournier and Galatola [27] for the pressure ΔP describing the entry of a vesicle in a cylindrical micropipette of radius s:

$$\Delta P = 2\gamma\left(\frac{1}{s} - \frac{1}{R_1} + \frac{\Gamma}{\gamma s}\right). \qquad (4)$$

Again, we clearly see here how the adhesion energy triggers a suction pressure via the term $\Gamma/\gamma s$, which was neglected in the original work of Evans and Yeung [17]. While Eq. (3) is useful for a variety of theoretical investigations, it is not sufficient to compute the positions of the contact lines $\mathbf{x}_1$ and $\mathbf{x}_2$. To close our formulation, we need to enforce the volume conservation of the vesicle during the permeation process. Considering a spherical vesicle of radius R, this implies $4\pi R^3/3 = \sum V_i^c + V^t$, where V_i^c is the volume of the spherical caps $(i = 1,2)$ and V^t is the volume of the section of the vesicle confined in the pore throat. The former can conveniently be expressed in terms of angles α_i made between the radius of the vesicle at the point of contact and the horizontal axis (Fig. 1) as $V_i^c = \pi r(z_i)^3 h(\alpha_i)/3$, with $h(\alpha_i) = [2 + 3\sin(\alpha_i) - \sin^3(\alpha_i)]/\cos^3 \alpha_i$. Further noticing that $\rho_i r_i = \cos \alpha_i$, the complete system of equations describing the equilibrium of an incompressible vesicle confined in a pore

is comprised of Eq. (2) and the volume conservation equation in the form

$$2\gamma\left(\frac{\cos \alpha_2}{r(z_2)} - \frac{\cos \alpha_1}{r(z_2)}\right) = \Delta P, \qquad (5)$$

$$\frac{\pi}{3}\sum_{i=1}^{2}[r(z_i)^3 h(\alpha_i)] + \int_{V_c} dV = \frac{4}{3}\pi R_v^3, \qquad (6)$$

with $\alpha_i = \theta + \arctan[r'(z_i)] - \pi$. This nonlinear system admits the coordinates z_i of the two contact lines as the solution (when this solution exists), given a pressure drop ΔP across the pore.

For convenience and ease of analysis, it is preferable to nondimensionalize the above equations. For this, note that the above system has the general form $g = \Delta P - f(\gamma,s,\theta,R,\mathbf{x}) = 0$, where the parameters in f describe the physical properties of the vesicle-pore complex. Scaling forces and lengths by γ and s (the pore aperture), respectively, the Buckingham π theorem states that our problem can be cast in the form $\Delta P^* = \frac{\Delta P s}{2\gamma} = \tilde{f}(\theta, \frac{R}{s}, \frac{\mathbf{x}}{s})$. In other words, we define a normalized vesicle radius $R^* = R/s$ and pore coordinate $z^* = z/s$ such that

$$\Delta P = \frac{2\gamma}{s}f(\theta, R^*, z^*). \qquad (7)$$

Implicitly, this relation states that the permeation pressure depends on vesicle deformability, which we measure here as the pressure difference across its surface. Indeed, a larger surface tension will increase this pressure difference, making vesicles appear less deformable and exhibit more resistance to pore permeation. In contrast, a larger pore size reduces the permeation pressure by increasing the length scale of the system. A larger curvature indeed yields a lower pressure within the vesicle and hence a lower resistance to deformation.

III. ANALYSIS OF VESICLE INSTABILITY AND CRITICAL PERMEATION PRESSURE

Numerous experimental observations show that vesicle deformation and permeation across a pore are largely dependent on both pore geometry [44] and vesicle adhesion [4]. We aim here to closely investigate these relationships by concentrating on a restricted, yet ubiquitous, set of pore morphologies found in microfluidic devices [45], micropipette aspiration studies [46], filtration membranes [47], and particle trapping devices [15]. The generic axisymmetric pore is described by a tapered hyperelliptical profile with semimajor and semiminor axes of length a and b, a shape factor n that controls the pore curvature, and a slope factor m that controls its asymmetry. The parametrization is written

$$r(z) = a\left(1 + \frac{m}{b}z\right)\left[\left(1 - \left|\frac{z}{b}\right|\right)^n\right]^{1/n} - r_L, \qquad (8)$$

where $2r_L$ is the exterior diameter of the pore (Fig. 1). As shown in Fig. 2, the shape of the pore ranges from a cylindrical channel of height $2b$ for $n \to \infty$ to a toroidal pore with an ellipsoidal section of axis a,b when $n = 2$. The slope factor further introduces an asymmetry to the pore such that $m = 0$ exhibits a symmetrical top-bottom shape, while more
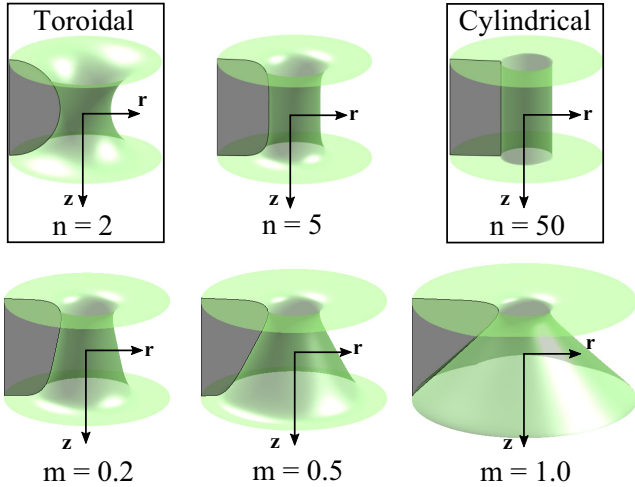
FIG. 2. Three-dimensional representation of the axisymmetric pore. In the top three figures, the value of m is kept constant at 0 while we vary the sharpness parameter n. In the bottom figures n is constant and equal to 5 while m is varied.

pronounced conical shapes are obtained as the magnitude of m increases; Eq. (8) can be used into the system of (5) and (6) to obtain an explicit form of the governing equations and a numerical solution for a variety of pore-vesicle systems (details are provided in Appendix A).

A. Equilibrium diagrams

The equilibrium states of a soft vesicle confined in a pore can be visualized by the pressure diagram, showing the position of the center of mass of the vesicle in terms of the pressure drop ΔP across the pore. Figures 3(a) and 3(b) show such diagrams for a normalized radius $R^* = 1.5$, adhesion energy $\Gamma = 0$, and toroidal and cylindrical pore geometries. It can be seen that for symmetric pores ($m = 0$) and nonwetting vesicles (solid lines), the diagram possesses three distinct regions (ascending, descending, and ascending), delimited in order by the maximum and the minimum values of the pressure drop ΔP. The first region starts when the vesicle is tangent to the pore in its underformed configuration (point A_1), which corresponds to a zero pressure drop. As the pressure increases, the vesicle enters the pore following the A_1-C_1 branch until it reaches the maximum pressure at C_1. In a pressure controlled system, this point yields to an instability where the vesicle, under an infinitesimal pressure increment, would dramatically leave the pore space by rapidly transforming its stored elastic energy into kinetic energy [forward motion in Fig. 3(a)]. This behavior is typically observed in the micropipette aspiration of neutrophils and the values of the critical pressure have been well estimated using a similar approach [40,48]. In a displacement driven system, however, the motion of the vesicle towards the pore center A_3 (region 2) would require a decrease in pressure until it reaches point C_2 and eventually A_2 as it exists the pore. For backward motion (the vesicle starts from the bottom of the pore), the first contact occurs in A_2 and the vesicle encounters its instability at C_2, both of which are analogous to A_1 and C_1. For a cylindrical pore, the pressure diagram displays similar trends with two notable differences:

(i) the A_1-C_1 and A_2-C_2 branches are steeper owing to the fact that a sharper pore opening requires a larger vesicle deformation and (ii) the flat region around A_3 corresponds to a situation where the vesicle is free to slide along a cylindrical channel without pressure variations.

The nature of the pressure curve is reminiscent of the equilibrium diagram of a ball on a hill that first requires energy to reach the top, but that restitutes this potential energy as it loses elevation. Following this analogy, we take an energetic approach wherein the stored mechanical energy in the vesicle is expressed as the difference ΔE in surface energy between the deformed and undeformed vesicle configurations. For an axisymmetric vesicle, this is expressed by

$$\Delta E = \gamma \left(\sum S_i - S_0 - 2\pi \int_{z_2}^{z_1} r(z) \cos \theta(z) dz \right), \quad (9)$$

where $S_0 = 4\pi R^2$ is the initial surface area of the vesicle and $S_i = 2\pi r(z_i)^2 (1 - \sin \alpha_i)/ \cos(\alpha_i)^2$ are the surface areas of top and bottom spherical caps. We observe here that for nonwetting vesicles ($\theta = \pi$), this energy is proportional to an increase in the vesicle's surface area due to deformation. The normalized energy landscapes ($\Delta E^* = \Delta E/\gamma S_0$) in Figs. 3(c) and 3(d) clearly show that as the vesicle moves forward and deforms, energy must be provided until it reaches the center point $z = 0$, while energy is restituted afterward. We also note that the A_1-C_1 branch is stable (concave region), the C_1-A_3 branch is unstable (convex region), and the inflection point C_1 denotes the onset of instability. We finally observe that point A_3 corresponds to a metastable equilibrium with maximum mechanical energy (largest vesicle deformation); any small deviation in pressure would therefore push the vesicle towards A_1 or A_2. It can also be seen that for a cylindrical pore ($n = 50$) the energy is constant around A_3 since no additional force has to be provided to deform the vesicle in the cylindrical section of the pore. Additionally, these energy diagrams provide important information regarding the direction of motion of the vesicle. In the absence of an external pressure, a vesicle will move towards the closest minimum energy point until it reaches an equilibrium position. The dynamics of motion involves complex processes such as internal fluid flow [18] and/or the appearance of a lubrication layer [49] between the vesicle and the pore, whose study is beyond the scope of this paper.

B. Role of adhesion

Adhesive pore-vesicle complexes display very different pressure and energy landscapes compared to their nonwetting counterparts. This effect, shown in Fig. 3 with dashed lines for an adhesion energy $\Gamma/\gamma = -0.19$, is twofold: (a) The pore exerts a suction pressure $\Delta P_{\text{suct}} < 0$ as the vesicle first touches the pore (point D_1') and (b) the system displays several equilibrium positions whose number and stability strongly depend on the pore shape. In particular, for both toroidal and cylindrical geometries, we find that when a vesicle becomes in close proximity to the entry point, it will naturally enter the throat to reach the equilibrium position A_1' (or A_2' for backward entry). If a positive pressure is applied, the vesicle follows a stable branch until it reaches the local pressure maximum at C_1', similarly to a nonwetting vesicle studied above. By contrast, a
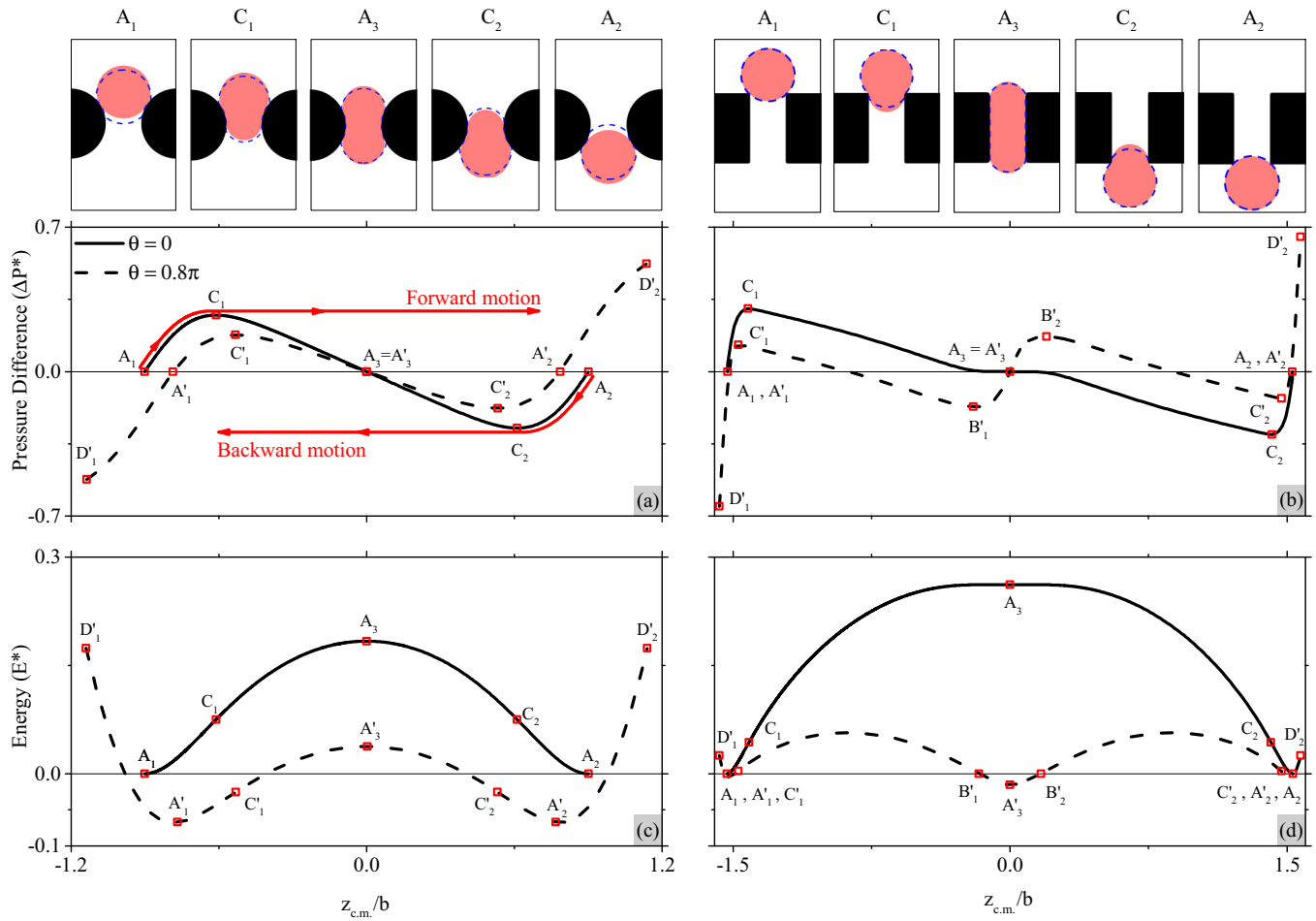
FIG. 3. Equilibrium and energy diagrams for two vesicles of radius $R^* = 1.5$ and adhesion energies $\Gamma = 0$ (solid lines) and $\Gamma = -0.19$ (dashed lines) in a toroidal ($n = 2$) and a cylindrical pore ($n = 50$) with $m = 0$ and $a = b = 2s$. (a) and (b) Variation of the equilibrium pressure with the relative position of the center of mass $z_{\text{c.m.}}/b$ for both vesicles in each respective pore. The A_i mark the locations of the points at 0 pressure, C_i the maximum entry pressure, and B_i and D_i the local and absolute maximum suction pressure, respectively. The section of the most relevant positions is show in the top insets. The red lines show the path followed by a pressure-driven vesicle in both directions. (c) and (d) Variation of the energy with the relative position of the center of mass $z_{\text{c.m.}}/b$ and the corresponding position of each point.

pressure increment at this point would not push the vesicle out of the pore but rather move it to the next equilibrium branch, C_2'-A_2' for the toroid or A_3'-B_2' for the cylinder. A much larger pressure ΔP_{suct} needs to be applied to completely remove the vesicle from the pore at D_2'. It can therefore be concluded that for a partially wetting vesicle in a toroidal pore, the critical permeation pressure is the maximum of $\Delta P(C_1')$ and $\Delta P(D_2')$. Interestingly, when the pore changes from toroidal to cylindrical, point A_3' changes from an unstable to a stable position. In other words, during its permeation, the vesicle may jump from one stable position to another (A_1' to A_3' to A_2') until it is allowed to leave the pore when the maximum pressure at D_2 is applied. The permeation pressure is now determined by the competition between $\Delta P(C_1')$, $\Delta P(D_1')$, and $\Delta P(B_2')$.

C. Critical permeation pressure

A number of experimental and theoretical studies [18,19,22,25,50] have focused on evaluating the maximum pressure drop [critical permeation pressure (CPP)] for a vesicle to go through (i.e., enter and exit) a pore. The distinction

between pore entry pressure (EP) and CPP is however not explicit in these studies and the effects of pore throat geometry (rather than opening) and adhesion are often neglected. Here we aim to show that these effects are in fact critical to the physics of vesicle permeation and/or trapping and that it is possible to tune the pore geometry and chemistry to achieve desired behaviors. We have seen in Figs. 3(a) and 3(b) that two quantities become particularly important when studying the CPP: the maximum EP at C_1 (or C_2 for backward motion) and the maximum exit pressure (XP) at D_2 (or B_2) that typically increases with adhesion energy. Generally, the CPP can therefore be defined as the maximum between the EP and the XP; Fig. 4(a) illustrates this relation for a cylindrical pore ($n = 50$), where the maximum of the equilibrium diagram (CPP) shifts from the EP to the XP as the contact angle is decreased from π to $\pi/2$. Figure 4(b) further shows that the relationship between CPP and adhesion is not trivial and it is dictated by the pore-vesicle interactions during either the entry or the exit of the pore. Four main regimes are observed, each of them associated with one of the four types of equilibrium diagrams depicted in Fig. 4(a): For small adhesion energies
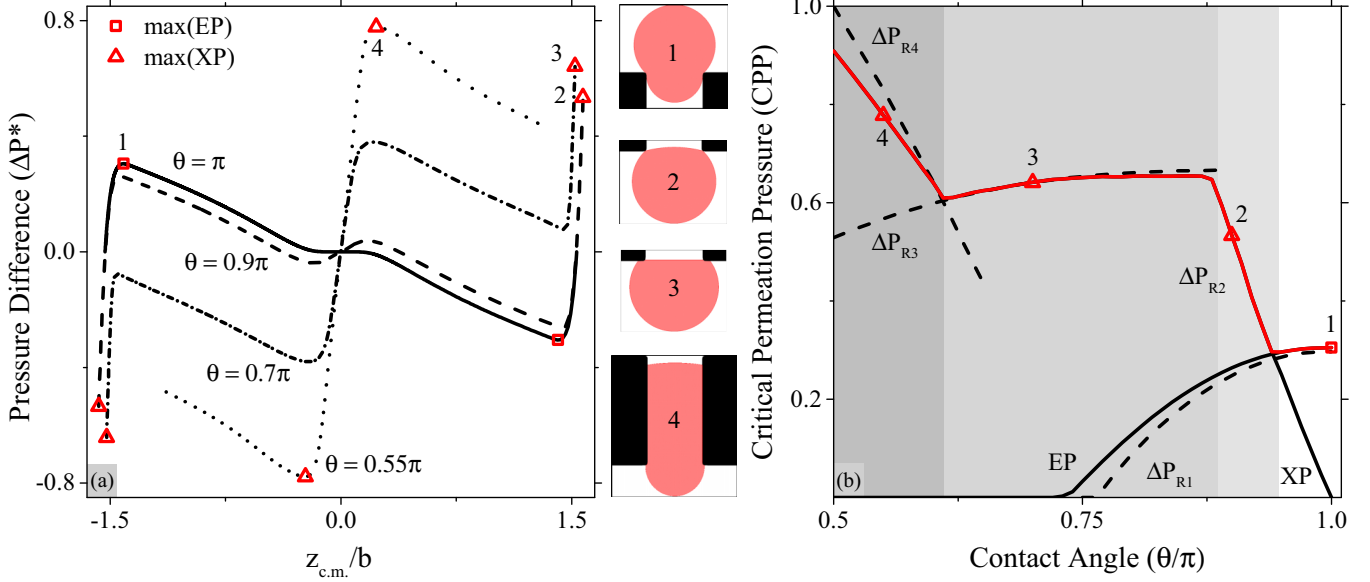
FIG. 4. (a) Equilibrium diagrams of four vesicles of the same relative size $R^* = 1.5$, but with different adhesion energies corresponding to $\theta = 0.55\pi, 0.7\pi, 0.9\pi$, and π, in a pore with geometrical properties $n = 50$, $a = b = 2s$, and $m = 0$. The position of maximum entry pressure has been labeled with a square, while the exit pressure has been labeled with a triangle. (b) Critical permeation pressure, the maximum of EP and XP, plotted versus the adhesion energy θ for the permeation of a vesicle with relative size $R^* = 1.5$ in a cylindrical pore with $n = 50$, $a = b = 2s$, and $m = 0$. The graphic displays four different regimes depending on the permeation mechanism of the vesicle, which have been differentiated by the vertical shading. In each of them, there is an inset showing an example of the position of the vesicle when the critical pressure was achieved. The dotted lines show the analytical expressions derived for this problem in its range of validity.

(contact angle near $\theta = \pi$), the critical pressure is dictated by the EP (Fig. 4, inset 1), which for a perfectly cylindrical channel can be expressed in terms of the contact angle as [22]

$$\Delta P_{R1}^* = \cos\theta \left[\left(\frac{2 - 3\cos\theta + \cos^3\theta}{\sin\theta - \sin^3\theta - 4R^{*3}\cos^3\theta - 2} \right)^{1/3} - 1 \right] \tag{10}$$

and which occurs at C_1, highlighted with a square in Fig. 4. As the adhesion energy increases, the equilibrium diagrams shift to the point where the pressure at C_1 coincides with D_2 in Fig. 4(a), the mechanism of vesicle permeation becomes *capillary driven*, i.e., CPP = XP (red triangles in Fig. 4). The next three regimes are therefore dominated by XP, rather than the entry pressure. In the second regime, for low to intermediate adhesion energies, the model shows that the vesicle exits the pore via a peculiar mechanism in which both contact lines merge, yielding no room for pore-vesicle contact. This corresponds to the maximum of an equilibrium diagram such as the one with $\theta = 0.9\pi$ in Fig. 4(a), where the vesicle shape is described by two coexistent spherical caps of different radii that are barely in contact with the pore as shown in Fig. 4, inset 2. In this regime, the pressure coincides with the expression previously calculated for the case when $\mathbf{x}_1 = \mathbf{x}_2$:

$$\Delta P_{R2}^* = -2 \frac{\sin(\beta)\sin\theta}{r^*(z)}, \tag{11}$$

until the mechanism drastically switches to regime 3. Indeed, for intermediate values of the adhesion energy, the model shows that the loss of vesicle equilibrium occurs through a flattening of its upper cap while remaining in contact with the lower portion of the pore (Fig. 4, inset 3). As the top curvature

vanishes, the force balance (2) on the vesicle can no longer be satisfied, forcing the particle out of the pore space. In this situation, the critical pressure can be analytically approximated by considering a single spherical cap whose contact line radius is larger than the pore aperture:

$$\Delta P_{R3}^* = \frac{1}{R^*}[(1 - \cos\theta)(\sin^2\theta + 1 - \cos\theta)/4]^{1/3}, \tag{12}$$

This expression (derived in Appendix B) agrees reasonably well with our numerical solution at $n = 50$. Note that despite the fact that the associated equilibrium diagram in Fig. 4(a) has its maximum in a very similar position, the CPP evolution is quite different due to a different exit mechanism. Finally, for a contact angle approaching $\pi/2$, yet another exit mechanism is predicted by the model. Here the adhesive interaction is so strong that the pressure required to exit its stable position at A_3' [Fig. 4(a), point 4], becomes larger than the suction pressure at D_2'. This means that the vesicle is forced out of the pore without settling in its stable position at A_2'. In this case, the CPP can be analytically approximated by (derivation in Appendix B)

$$\Delta P_{R4}^* = \sin(\theta) + \cos(\theta). \tag{13}$$

We note here that the small discrepancy between this expression and numerical results observed (region 4 in Fig. 4) is due to the fact that the above solution is based on an opening curvature ($n \to \infty$), while the numerical solution is based on a finite value of the curvature (n).

D. Asymmetric pores

Asymmetric pores can be designed to enable easy vesicle permeation in one direction but block their entry in the other
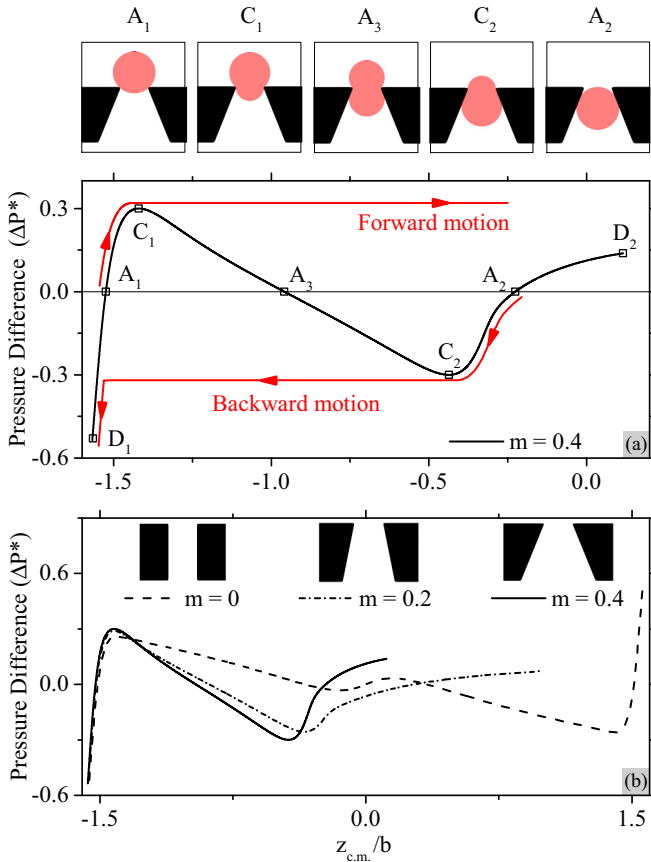
FIG. 5. (a) Equilibrium diagram of a vesicle with radius $R^* = 1.5$ and contact angle $\theta = 0.9\pi$ inside a pore with $m = 0.4$, $a = b = 2s$, and $n = 50$. The relevant positions of the vesicle have been labeled, with A_1, A_2, and A_3 the positions at zero pressure, C_1 and C_2 the entry pressure, and D_1 and D_2 the exit pressure. (b) Equilibrium diagrams for the cases where $m = 0, 0.2$, and 0.4 for the same contact angle to illustrate the effect of pore asymmetry on the curves' evolution.

[51]. For instance, Guo *et al.* [52] showed that the critical pressure of cells in conical pores depends on their direction and its value is well estimated by the present model. In Fig. 5(a) we show the typical vesicle deformation and the associated pressure diagram for a conical pore whose slope parameter is $m = 0.4$ (other relevant parameters are $n = 50$, $R^* = 1.5$, and $\Gamma/\gamma = -0.05$). A few key observations can be made related to the pore asymmetry. (i) The equilibrium diagram is no longer symmetric since the entry and exit mechanisms are different depending on whether a vesicle moves forward or backward into the pore. (ii) Since vesicle entry is almost exclusively driven by the geometry of the pore mouth but not its throat, the pressure diagram is almost unaffected by the pore asymmetry before EP is reached. A similar EP is therefore observed for cylindrical and conical pores with the same entry radius s and curvature (or shape factor n) as shown in Fig. 5(b). (iii) The XP is strongly affected by pore asymmetry. Indeed, for this system, the XP (pressure at D_2) is around 0.1 for a vesicle moving forward, while it is on the order of 0.5 for a vesicle moving in the reverse direction. To understand the consequences of these observations, consider a vesicle undergoing a forward-backward cycle into the pore [Fig. 5(a)]. On its way forward,

the vesicle first reaches its equilibrium position at $\Delta P = 0$ before it slowly moves into the pore under increasing pore pressure. The entry instability is reached at point C_1, after which any additional increase in pressure forces the vesicle out of the pore, since the XP is less than the EP. In other words, the forward permeation pressure is $CPP^+ = EP \approx 0.3$ in this system. On its way backward, the vesicle first settles in its equilibrium position at A_2 before it is forced into the pore under a negative pressure drop. After reaching the entrance instability at C_2, the vesicle jumps into the next equilibrium branch. It will finally be forced out of the pore if the pressure drop exceeds (in magnitude) the XP at D_1. For backward motion, the critical permeation pressure is therefore $CPP^- = XP \approx 0.5$ in this system. Figure 5(b) shows that the pressure diagram, particularly the region corresponding to the exit mechanism, is very sensitive to the slope of the conical pore. This implies that the geometric design of the pore can be harvested to tune the difference between the CPP for forward and backward motion, a feature that is important, for instance, for designing microfluidic diodes.

IV. VESICLE SEPARATION, TRAPPING, AND PROFILING

The design of pores that are capable of targeting specific particles for fractionation, separation, and trapping is key to a number of technological applications. We focus here on three important problems in membrane science, vesicle profiling, and the design of microfluidic diodes for complex fluids and colloids.

A. Vesicle separation

In membrane filtration or separation techniques [53], we aim to separate populations of deformable particles using criteria such as size, deformability, or adhesion properties. We ask here whether it is possible to design pore geometries, characterized by their aperture size $s/R = 1/R^*$ and curvature (or shape parameter n), in order to achieve very distinct CPPs for two vesicle populations. For this, we first investigate the effect of curvature at a fixed relative vesicle size by varying the pore shape from a toroidal shape ($n = 2$) to a cylindrical shape ($n = 50$) and determined the CPP for a range of contact angles $\pi/2 \leqslant \theta \leqslant \pi$ as shown in Fig. 6(a). We find that smoother, more rounded pores tend to (a) decrease the CPP for all ranges of adhesion and (b) shift the transitions between different permeation regimes to the left. This trend is particularly true for toroidal pores ($n = 2$) where the mechanism associated with (13) completely disappears. To understand the effect of pore aperture, we performed a similar study by varying R^* at fixed pore curvature $n = 2$ [Fig. 6(b)]. The model shows that pore aperture and vesicle adhesion play two competing roles during the permeation process. For low adhesion, the process is dominated by the EP required to deform the vesicle into the pore; this explains why the CPP increases sharply with vesicle size in this region [right-hand side of Fig. 6(b)]. By contrast, for larger adhesion, the process becomes dominated by capillary effects (i.e., XP). Interestingly, we find that this pressure decreases with increasing vesicle size (or decreasing aperture) and that this phenomenon yields an inversion of the trends: Small apertures yield a smaller CPP. This observation can be understood by looking at the force balance on the vesicle
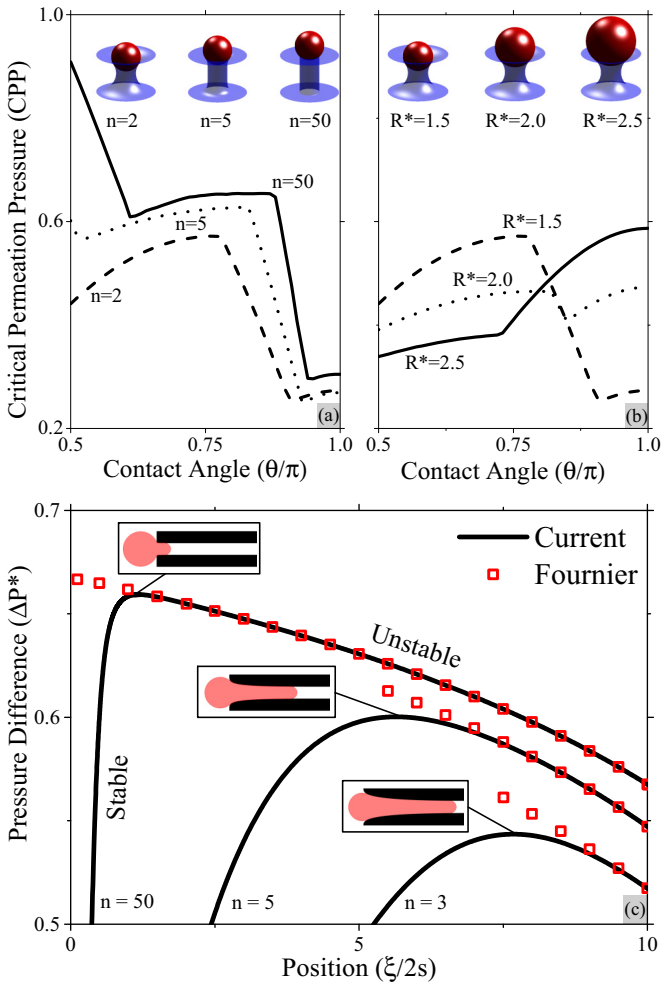
FIG. 7. Schematic of the forces acting on the vesicle. The resultant from the tension on each cap T_i is directly proportional to its curvature and tangent to the contact point. These surface forces are balanced by the resultant of the pressure difference across the interface $P_{\mathrm{in}} - P_i$.

FIG. 6. The CPP variation with the contact angle θ in (a) three different pore shapes ($n = 2,5,50$) with $a = b = 2s$, $m = 0$, and a vesicle of $R^* = 1.5$ and (b) three different values of the relative vesicle size ($R^* = 1.5,2.0,2.5$) on a toroidal pore ($n = 2$) with $a = b = 2s$ and $m = 0$. For clarity, six insets depict the shape of each pore with the respective vesicle tangent to them. (c) Detail of the equilibrium diagram for three different pores with $a = 2s$, $b = 20s$, and $n = 3,5,50$, for the same vesicle ($R^* = 1.5$ and $\Gamma = 0$) and its comparison by the solution proposed by Fournier and Galatola for the equilibrium pressure in a cylindrical pore. The vesicle's position is determined here by the distance (ξ) of its leading edge inside the pore. Three insets depict the position of the vesicle at the moment when the EP is achieved. Note that the volume of the axisymmetric vesicle remains constant regardless of its configuration and despite the apparent change in projected areas seen in the figures.

as shown in Fig. 7. In the case of high adhesion, the curvature of the inner cap is typically small compared to that of the outer cap (see insets 2–4 in Fig. 4). This implies that vertical forces pulling the vesicle inward mostly arise from the surface tension in the outer cap. Since capillary forces are proportional to curvature, smaller vesicles (or increasing apertures) tend to display a higher resistance to exit the pore. With these competing mechanisms, we observe that for a toroidal pore, the CPP curves for different vesicle sizes intersect at a value close to $\theta \approx 0.8\pi$. In other words, two vesicles with equal surface tension and adhesion but different sizes can exhibit the same CPP.
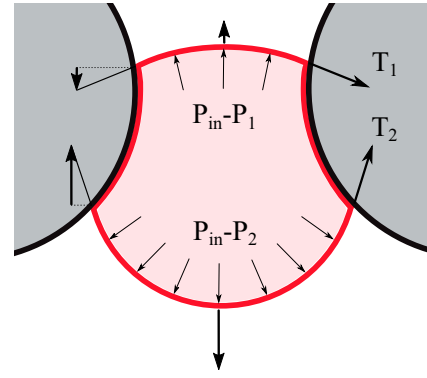
Valuable insights can be gained from the above predictions. For instance, two particles with the same surface tension but different size and adhesion can be separated by properly designing a pore that ensures a very distinct CPP. This strategy can further be optimized by altering the wetting properties of pores with techniques such as electrowetting [26]. In the context of deformability-based particle separation [12,13,25], we note that our predictions are for normalized pressure $\Delta P^* = \Delta Ps/2\gamma$, implying that pore opening s and surface tension must also be accounted for to distinguish between two particles with different mechanical properties. Dimensional versions of the diagrams presented in Fig. 6 may therefore be preferable for design purposes.

B. Vesicle profiling

Quantitative observations of particle deformation in narrow pores [21] and micropipettes [54] have traditionally been used as a method to indirectly measure their physical properties. We here concentrate on micropipette aspiration for which standard experiments and modeling efforts have focused on cylindrical pipettes with constant cross sections. Using this technique, a relation between vesicle shape and suction pressure can be measured and used to estimate various properties such as surface tension, elasticity, or viscosity [55]. A typical issue, however, is that not all vesicles' equilibrium positions entering a micropipette are stable [19] and since the aspiration technique is pressure driven, a vesicle only remains stable when the suction pressure is below the EP. We have seen in Fig. 3(b) that for a cylindrical pore with a sharp corner, the EP is reached at very small vesicle deformation. In other words, this classical design suffers from two major drawbacks: (i) The deformation of the vesicle is highly sensitive to suction pressure, a feature that can affect the measurements' accuracy, and (ii) the vesicle's response can only be surveyed within the range of small deformation, which strongly restricts our ability to fully characterize its mechanical response. A solution to these limitations is suggested in Fig. 3(a), where we found that a more rounded pore tends to both postpone the EP and decrease the slope of the pressure-displacement curve. Based on this idea, we show in Fig. 6(c) the pressure diagram for
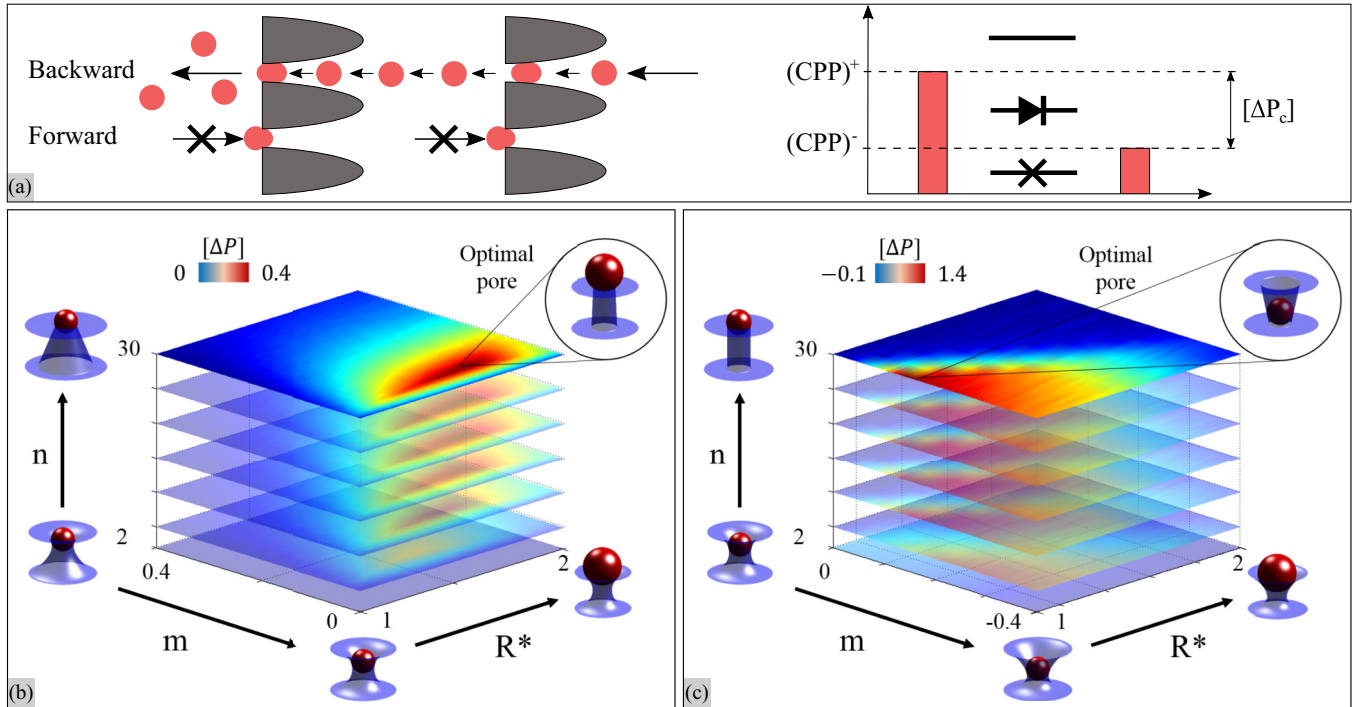
FIG. 8. (a) Scheme of a pore with a funnel shape that has a different critical pressure depending on what direction it is crossed, forward CPP^+ or backward CPP^-. The difference between these two is defined as the trapping efficiency $[\Delta P_c]$ and it indicates how probable it is to trap a vesicle using these technique. Four-dimensional maps showing the variation on axisymmetric pressure with the relative vesicle radius R^*, the slope m, and the shape parameter n are shown for two different vesicles: (a) with $\Gamma = 0$ and (b) with $\Gamma = -0.19$ ($\theta = 0.8\pi$). The red zones indicate where the axisymmetric pressure is positive and the pore traps particles on top. In contrast, the blue zones have a negative pressure asymmetry and vesicles are trapped on the bottom. A circled inset shows the optimal pore and corresponding vesicle in each case.

a cylindrical pipette whose mouth curvature is varied from $n = 50$ (very sharp) to $n = 3$ (very smooth). As expected, we find that decreasing n postpones the onset of instability, decreases the entry pressure, and allows one to probe the vesicle for a larger range of deformation by making it less sensitive to shape changes. In these regimes, however, we note that the predictions of standard models, such as that proposed by Fournier and Galatola [27], are limited to the unstable branch of the pressure diagram [shown by squares in Fig. 6(c)] and become less accurate as n decreases. Semianalytical approaches, such as that discussed in this paper, therefore would need to be used in combination with new pipette designs (based on smooth mouth opening) to better probe the properties of vesicles and other soft colloidal particles. Note that certain colloidal particles (bacteria and cells, for instance) may display more complex mechanical behaviors and remain stable under the classical pipette aspiration tests [48]. In these cases, a more thorough analysis can be performed to identify pipette designs that enable a better characterization of their properties.

C. Microfluidic diodes

The concept of a fluid diode has been long used in microfluidics [16,56,57] with applications in biomedical engineering. The separation of particles that exhibit distinct mechanical properties from their surroundings have motivated the design of asymmetric microfluidic devices that can sort soft and rigid particles under oscillatory flow [14,15,52]. To examine the

role of pore geometry in particle trapping, we propose here to define a measure of trapping efficiency as the difference $[\Delta P_c] = |\mathrm{CPP}^+| - |\mathrm{CPP}^-|$ between the CPP as a vesicle moves forward (superscript $+$) and backward (superscript $-$) through the pore [Fig. 8(a)]. With this definition, it is clear that the sign of $[\Delta P_c]$ defines the trapping direction: If $[\Delta P_c] > 0$, vesicles are trapped on the top side of the pore (forward diode), while if $[\Delta P_c] < 0$, they are trapped on the bottom (backward diode). Figure 8(a) also illustrates the range of pore pressures ($\mathrm{CPP}^- \leqslant \Delta P \leqslant \mathrm{CPP}^+$) for such a diode to operate efficiently; pressures above CPP^+ allow the permeation of vesicles in both directions, while values below CPP^- do not allow particle permeation in any direction. We finally note that the symmetric pores studied in the previous section are inefficient at trapping particles since the antisymmetry of the pressure-displacement diagram implies $[\Delta P_c] = 0$.

To investigate the role of pore size, shape, and asymmetry in trapping efficiency, we performed a parametric study that consisted of sweeping the space (m, n, R^*) in order to obtain a three-dimensional graphical representation of the dependence $[\Delta P_c](m, n, R^*)$. Results for a nonwetting ($\Gamma = 0$) and an adhering ($\Gamma = -0.19$) vesicle are provided in Figs. 8(b) and 8(c), respectively. For convenience, we focused here on forward trapping, i.e., our study was restricted to $[\Delta P_c] \geqslant 0$. Trends in backward trapping can then be deduced by symmetrically inverting the system. The following key observations can be made regarding the trapping of nonwetting particles [Fig. 8(b)]. (i) The relationship between pore design

and trapping efficiency is nonlinear and exhibits an optimum. (ii) The optimal design is a slightly tapered (moderate n) conical shape. Indeed, we found that pronounced conical shapes (large m) would lose their "asymmetric power" by providing an overly restrictive pore opening. (iii) Trapping efficiency is promoted by larger pore curvatures, controlled by the shape parameter n. Figure 8(c) further shows that the mechanics of asymmetric trapping is strongly affected by adhesion. This observation can be explained by the fact that the CPP is dominated by the XP, which involves mechanisms very different from those associated with vesicle entry. In this case, the following pattern emerges. (a) The optimal pore is still a cone, but with a more pronounced slope. (b) The position of the optimal cone is reversed ($m < 0$) and to catch a vesicle on top we would need the opposite slope, which is not at all intuitive. (c) The optimal pore aperture is smaller with adhesion. This is a consequence of the different regimes dominating the XP on each side of the pore. As can be seen in Fig. 6, small vesicles indeed have larger values of XP, which clearly end up dominating the system.

The above analysis could have far reaching potential in the design of membranes, microfluidic devices, and fluidic diodes for complex fluids. The three-dimensional maps shown in Fig. 8 directly pinpoint the design that offers the highest trapping efficiency for a given particle in order to devise deformability-based systems aimed to separate particles of similar size and adhesion. These maps, however, need to be complemented by the knowledge of the actual dimensional values of CCP$^+$ and CPP$^-$ in order to precisely determine the operating pressure corresponding to the device. This can be achieved by reversing the nondimensional framework.

V. CONCLUSION

We have derived a set of nonlinear equations that can describe the permeation of surface-tension-dominated adhering vesicles in arbitrary axisymmetric pores. We found that this problem can be studied in terms of pressure and energy landscape that exhibit various equilibrium positions and mechanical instabilities as the vesicles penetrate, travel through, and exit from the pore. Interestingly, the maximum pressure for vesicle permeation (CPP) is highly dependent on the mechanisms by which the vesicle interacts with the pore and in particular their adhesion energy. In particular, model predictions showed that capillary effects produced by vesicle adhesion can play a significant role by creating a suction pressure (XP) that tends to retain the vesicle within the pore. Eventually, vesicles with even slightly different adhesion properties can display significant changes in their permeation abilities. Overall, the results presented in this paper show that one can optimize the design of microfluidic devices, diodes, and membranes to specifically target populations of colloids based on their size, surface tension, and adhesion properties.

ACKNOWLEDGMENTS

APPENDIX A: SOLUTION PROCEDURE

Let us consider the problem of a vesicle trapped in an axisymmetric pore spanning in the z coordinate from $-b$ to b and whose geometry is given by (8). The solution is found by solving the system of equations $\boldsymbol{R}$ formed by Eqs. (5) and (6). However, the solution to this system is not trivial since (i) it is highly nonlinear and (ii) each value of the pressure drop ΔP leads to multiple solutions for the vesicle position. The latter issue can be simply addressed by enforcing the z coordinate of one of the contact lines z_i and solving for the corresponding pressure drop and the second detachment point. This operation may be thought of as a *displacement-driven* boundary condition, known to be more stable than a *force-driven condition* for mechanical systems displaying unstable behaviors. The solution of the system is then expressed as the optimization problem $\min[\mathbf{R}(\mathbf{u}), \mathbf{u} \in \mathcal{F} = \{\mathbf{u} : \mathbf{u}_{LB} \leqslant \mathbf{u} \leqslant \mathbf{u}_{UB}\}]$, where $\mathbf{u}_{LB}$ and $\mathbf{u}_{UB}$ are the upper and lower bounds of the solution. The nonlinearity of the system is primarily caused by the arbitrary definition of the geometry $\mathbf{r}(z)$. This implies that, in general, one cannot find a closed form expression for the enclosed volume of the vesicle and the term $\int_{V_c} dV$ in (6) has to be computed numerically. This has been done by dividing the central volume in N horizontal slices and using a trapezoidal rule

$$V_c = \int_{z_1}^{z_2} \pi [r_L - r(z)]^2 dz \tag{A1}$$

$$= \sum_{k=1}^{N} \left(\pi (r_L - r_m)^2 \frac{|z_{k+1} - z_k|}{2} \right), \tag{A2}$$

where r_m is the average between r_{k+1} and r_k. Hence, since finding a general analytical solution is not possible, we used a trust-region-reflective algorithm with an initial approximation $\mathbf{u}_0 = \{z_i = b, \Delta P = 0\}$ and a tolerance of $\|\mathbf{R}\| = 10^{-12}$. This algorithm is widely implemented in multiple platforms and one can use, for instance, the function lsqnonlin built in MATLAB.

APPENDIX B: DERIVATION OF ANALYTICAL SOLUTIONS ON A CYLINDRICAL CHANNEL

In a cylindrical pore, one can find analytical solutions for the exit pressure similar to the ones that Nazzal and Wiesner derived for the entry pressure. We derive here the corresponding expressions for the exit pressure in regimes 3 and 4, which correspond to Eqs. (5) and (6). Note that these are approximate results that will match our model when the pore has a sharp transition at the edge $n \rightarrow \infty$.

1. Regime 3

The exit mechanism of the vesicle in this regime occurs when the top cap becomes perfectly flat ($\rho_1 = 0$) so the force balance cannot be satisfied beyond this point. For a nonwetting vesicle and a cylindrical pore, this can only happen when z_1

is right at the edge of the cylinder (the curvature is constant within its walls). In that scenario, the vesicle is equivalent to a droplet on a flat surface and we can find our solution by equating the original volume to a spherical cap resting on a flat surface:

$$V_0 = V_{\text{cap}}, \tag{B1}$$

$$\frac{4}{3}\pi R_0^3 = \frac{1}{3}\pi \frac{1}{\rho_2^3}(2 - 3\cos\theta + \cos^3\theta), \tag{B2}$$

so we obtain $\rho_2^3 = (1 - \cos\theta)(\sin^2\theta + 1 - \cos\theta)/4R_0^3$. The Laplace law in this particular case is simply $\Delta P^* = \rho_2$ and by introducing the value of the curvature we directly obtain Eq. (12).

2. Regime 4

This exit mechanism occurs when the contact angle approaches $\pi/2$ and the value of the curvature inside the cylinder tends to zero. In this situation, the force opposing the external pressure arises from the bottom cap and it will reach its maximum when its radius is minimum. In a cylindrical pore the minimal radius is equal to the pore radius s and can only occur when the lower detachment point is exactly at the pore edge $z_2 = -b$ and $R_2 = s/\sin(\theta)$. The top cap is then inside the cylindrical channel and constrained by its walls, so its radius is simply $R_1 = s/\cos(\theta)$. By normalizing these quantities and introducing them into the Laplace law we obtain the analytical expression for regime 4:

$$\Delta P^* = \cos\theta + \sin\theta. \tag{B3}$$

[1] M. Cheryan, Membr. Technol. **2005**, 5 (2005).
[2] J. Mueller, Y. Cen, and R. H. Davis, J. Membr. Sci. **129**, 221 (1997).
[3] H.-Y. Li, C. D. Bertram, and D. E. Wiley, AIChE J. **44**, 1950 (1998).
[4] E. N. Tummons, V. V. Tarabara, J. W. Chew, and A. G. Fane, J. Membr. Sci. **500**, 211 (2015).
[5] K. Pantel, R. H. Brakenhoff, and B. Brandt, Nat. Rev. Cancer **8**, 329 (2008).
[6] S. Stott, R. Lee, and S. Nagrath, Sci. Transl. Med. **2**, 25ra23 (2010).
[7] P. Xue, Y. Wu, J. Guo, and Y. Kang, Biomed. Microdev. **17**, 39 (2015).
[8] T. A. Desai, D. J. Hansford, A. H. Nashat, G. Rasi, J. Tu, Y. Wang, M. Zhang, and M. Ferrari, Biomed. Microdev. **2**, 11 (2000).
[9] W. Beattie, X. Qin, L. Wang, and H. Ma, Lab Chip **14**, 2657 (2014).
[10] W. A. Lam, M. J. Rosenbluth, and D. A. Fletcher, Brit. J. Haematol. **142**, 497 (2008).
[11] H. Mohamed, M. Murray, J. N. Turner, and M. Caggana, J. Chromatogr. A **1216**, 8289 (2009).
[12] G. Hvichia, Z. Parveen, C. Wagner, M. Janning, J. Quidde, A. Stein, V. Müller, S. Loges, R. Neves, N. Stoecklein, H. Wikman, S. Riethdorf, K. Pantel, and T. Gorges, Int. J. Cancer **138**, 2894 (2016).
[13] P. Preira, V. Grandné, J.-M. Forel, S. Gabriele, M. Camara, and O. Theodoly, Lab Chip **13**, 161 (2013).
[14] A. F. Sarioglu *et al.*, Nat. Methods **12**, 685 (2015).
[15] S. M. McFaul, B. K. Lin, and H. Ma, Lab Chip **12**, 2369 (2012).
[16] R. D. Sochol, A. Lu, J. Lei, K. Iwai, L. P. Lee, and L. Lin, Lab Chip **14**, 1585 (2014).
[17] E. Evans and A. Yeung, Biophys. J. **56**, 151 (1989).
[18] J. L. Drury and M. Dembo, Biophys. J. **76**, 110 (1999).
[19] J. Derganc, B. Bozic, S. Svetina, and B. Zeks, Biophys. J. **79**, 153 (2000).
[20] K. Akashi, H. Miyata, H. Itoh, and K. Kinosita, Biophys. J. **71**, 3242 (1996).
[21] X. Sun, W. D. Weinlandt, H. Patel, M. Wu, and C. J. Hernandez, Lab Chip **14**, 2491 (2014).
[22] F. F. Nazzal and M. R. Wiesner, Water Environ. Res. **68**, 1187 (1996).
[23] H. Bruus, *Theoretical Microfluidics* (Oxford University Press, Oxford, 2007).
[24] F. Y. Leong, Q. Li, C. T. Lim, and K.-H. Chiam, Biomech. Model. Mechanobiol. **10**, 755 (2011).
[25] Z. Zhang, J. Xu, B. Hong, and X. Chen, Lab Chip **14**, 2576 (2014).
[26] D. Baratian, A. Cavalli, D. van den Ende, and F. Mugele, Soft Matter **11**, 7717 (2015).
[27] J.-B. Fournier and P. Galatola, Soft Matter **4**, 2463 (2008).
[28] E. Evans and W. Rawicz, Phys. Rev. Lett. **64**, 2094 (1990).
[29] K. Allen Rodowicz, H. Francisco, and B. Layton, Chem. Phys. Lipids **163**, 787 (2010).
[30] D. Needham and R. Hochmuth, Biophys. J. **61**, 1664 (1992).
[31] U. Seifert, Z. Phys. B **97**, 299 (1995).
[32] U. Seifert, Adv. Phys. **46**, 13 (1997).
[33] W. Helfrich, Phys. Rev. A **39**, 5280 (1989).
[34] L. C. Foucard, J. Pellegrino, and F. J. Vernerey, Comput. Model. Eng. Sci. **98**, 101 (2014).
[35] A. D. Petelska, Cent. Eur. J. Chem. **10**, 16 (2012).
[36] G. Khelashvili, B. Kollmitzer, P. Heftberger, G. Pabst, and D. Harries, J. Chem. Theory Comput. **9**, 3866 (2013).
[37] J. J. Kwan and M. A. Borden, Soft Matter **8**, 4756 (2012).
[38] E. Dressaire, R. Bee, D. C. Bell, A. Lips, and H. A. Stone, Science **320**, 1198 (2008).
[39] K. D. Girard, C. Chaney, M. Delannoy, S. C. Kuo, and D. N. Robinson, EMBO J. **23**, 1536 (2004).
[40] D. V. Zhelev, D. Needham, and R. M. Hochmuth, Biophys. J. **67**, 696 (1994).
[41] P.-G. de Gennes, F. Brochard-Wyart, and D. Quere, *Capillarity and Wetting Phenomena* (Springer, New York, 2004), p. 291.
[42] P. Renvoisé, J. W. M. Bush, M. Prakash, and D. Quéré, Europhys. Lett. **86**, 64003 (2009).
[43] L. C. Foucard and F. J. Vernerey, Int. J. Numer. Methods Eng. **107**, 923 (2016).
[44] S. Kosvintsev, P. Sutrisna, I. Cumming, R. Holdich, and G. Mason, Chem. Eng. Res. Design **85**, 530 (2007).
[45] N. Champagne, R. Vasseur, A. Montourcy, and D. Bartolo, Phys. Rev. Lett. **105**, 044502 (2010).

[46] M. Szwast, T. Suchecka, and W. Piątkiewicz, Chem. Process Eng. **33**, 385 (2012).

[47] C. Dekker, Nat. Nanotechnol. **2**, 209 (2007).

[48] R. M. Hochmuth, J. Biomech. **33**, 15 (2000).

[49] D. G. Hunter and B. J. Frisken, Biophys. J. **74**, 2996 (1998).

[50] T. Darvishzadeh and N. V. Priezjev, J. Membr. Sci. **423-424**, 468 (2012).

[51] L. Gorre, E. Ioannidis, and P. Silberzan, Europhys. Lett. **33**, 267 (1996).

[52] Q. Guo, S. M. McFaul, and H. Ma, Phys. Rev. E **83**, 051910 (2011).

[53] T. F. Headen, S. M. Clarke, A. Perdigon, G. H. Meeten, J. D. Sherwood, and M. Aston, J. Colloid Interface Sci. **304**, 562 (2006).

[54] J. R. Henriksen and J. H. Ipsen, Eur. Phys. J. E **14**, 149 (2004).

[55] W. D. Merryman, I. Youn, H. D. Lukoff, P. M. Krueger, F. Guilak, R. A. Hopkins, and M. S. Sacks, Am. J. Physiol. **290**, H224 (2006).

[56] D. C. Leslie, C. J. Easley, E. Seker, J. M. Karlinsey, M. Utz, M. R. Begley, and J. P. Landers, Nat. Phys. **5**, 231 (2009).

[57] B. Mosadegh, C.-H. Kuo, Y.-C. Tung, Y.-s. Torisawa, T. Bersano-Begey, H. Tavana, and S. Takayama, Nat. Phys. **6**, 433 (2010).